

To appear ApJ 000,000.

GSH 138–01–94 , an old supernova remnant in the far outer Galaxy

J.M. Stil

and

J.A. Irwin

Queen's University, Kingston, ON K7L 3N6, Canada

stil@astro.queensu.ca

irwin@astro.queensu.ca

ABSTRACT

The properties of the Galactic H I shell GSH 138–01–94 are derived from data of the Canadian Galactic Plane Survey. The basic parameters of GSH 138–01–94 were determined by fitting the expansion of a thin shell to the expansion velocity field on the sky. The kinematic distance is 16.6 kpc for $v_{\text{LSR}} = -94.2 \pm 0.5 \text{ km s}^{-1}$. The radius is $180 \pm 10 \text{ pc}$, the expansion velocity $v_{\text{exp}} = 11.8 \pm 0.9 \text{ km s}^{-1}$, and the mass $2 \times 10^5 M_{\odot}$. No radio continuum counterpart of the shell was detected at 21 cm or at 74 cm. Absorption of a background continuum source constrains the spin temperature of H I in the shell to $T_s = 230_{173}^{367} \text{ K}$. The expansion age of GSH 138–01–94 is 4.3 Myr. These observables are in excellent agreement with predictions from hydrodynamic models for a supernova remnant in a low-density low-metallicity environment such as the outer Galaxy. GSH 138–01–94 is then the largest and the oldest supernova remnant known. It provides direct evidence for the release of mechanical energy in the interstellar medium by stars in the outer galaxy. It is argued that such old supernova remnants be found in low-density, low-metallicity environments such as the outer Galaxy, dwarf galaxies and low surface brightness galaxies.

Subject headings: ISM: bubbles, kinematics and dynamics, supernova remnants, Galaxy: kinematics and dynamics

1. Introduction

The rate and the location of star formation is an important factor in the energy budget of the interstellar medium and, in the long term, the evolution of galaxies. The gaseous disk in most galaxies is much more extended than the stellar disk, leaving a significant fraction of the mass of the interstellar medium at large radii outside the bright optical disk. Despite the significant gaseous mass at large radii, little or no star formation occurs outside the stellar disk.

The most widely accessible tracer of kinetic energy in the interstellar medium inside and outside the stellar disk of galaxies is the H I velocity dispersion, σ_{HI} . Remarkably, σ_{HI} remains constant, approximately 10 km s^{-1} , with distance from the centre, despite a drop of more than two orders of magnitude in the surface density of stars (Van Zee & Bryant 1999). Energy sources that have been proposed to sustain the $\sim 10 \text{ km s}^{-1}$ H I velocity dispersion in the outskirts of galaxies include previously undetected low-level star formation (Ferguson et al. 1998a), magneto-hydrodynamic instabilities in the disk (Sellwood & Balbus 1999), and infalling gas clouds (Hunter et al. 1998, 1999). Which of these, if any, is the dominant source of energy is still an open question.

In this paper we present evidence for supernova activity in the extreme outer region of our Galaxy. Evidence for star formation at large distances from the Galactic centre exists from detection of molecular gas, distant O and B stars, and their associated H II regions. In this paper, we present evidence for an expanding H I shell in the same area of the Galaxy as surveyed by Digel et al. (1994). The structure is visible in the Maryland-Greenbank survey map shown by Digel et al. (1994), but the southern half is so faint that it was not previously recognized as a shell.

2. Observations

2.1. The Canadian Galactic Plane Survey

The data presented in this paper were obtained as part of the Canadian Galactic Plane Survey. H I 21-cm line observations were carried out with the Dominion Radio Astrophysical Observatory (DRAO) interferometer, supplemented with zero-spacing information from the DRAO 26m telescope. These data represent all structure down to the $1' \times 1' / \cos \delta$ resolution

Fig. 1.— H I channel maps from the DRAO 21-cm line data. Every other channel between -78 km s^{-1} and -110 km s^{-1} is shown.

limit of the DRAO interferometer at 21 cm wavelength and declination δ . Additional observations of 21-cm continuum and 74-cm continuum from DRAO, and CO spectral line data from the Five College Radio Astronomy Observatory (FCRAO) were used. A description of these data sets can be found elsewhere (Higgs et al. 1999; Taylor et al. 1999; Heyer et al. 1998; Carpenter 1997).

3. Results

3.1. General morphology

Figure 1 shows the shell that we refer to as GSH 138–01–94, as a circular structure with radius 37.3, best visible in the channel maps around velocity -96 km s^{-1} . The blueshifted side of the shell represents the most extreme velocity of all H I in this direction. On the redshifted side of the shell, the confusion with the background is stronger. The channel maps between -88.0 km s^{-1} and -102.9 km s^{-1} display a distinct empty region surrounded by areas of higher intensity. The redshifted half of the shell is clearly fainter than the blueshifted half. However, the redshifted half shows several filamentary structures similar to blueshifted filaments that can be safely attributed to the shell. Examples of such features are found at $(l, b, v) = (138^\circ.3, -1^\circ.8, -89.7)$ and $(138^\circ.0, -0^\circ.7, -88.0)$. At an even more redshifted velocity the empty region inside the ring fills up to become a local maximum, most clearly visible in the channel maps of -81.4 km s^{-1} and -83.1 km s^{-1} , that disappears as the velocity decreases to -78 km s^{-1} . On the blueshifted side, the ring shape starts filling up in the channel maps at -106.2 km s^{-1} . Therefore, the change in morphology with velocity is symmetric with respect to the channel map at -94.6 km s^{-1} , although the redshifted side is somewhat fainter than the blueshifted side. This behavior is characteristic of an expanding shell, with both the near (blueshifted) and far (redshifted) sides visible. At the lowest intensity levels visible in Figure 1, the shell is nearly continuous, but the side that faces the Galactic equator is a factor 2 brighter than the opposite side, on average.

The shell is further illustrated in the latitude-velocity diagram in Figure 2. The redshifted emission that we associate with GSH 138–01–94 traces the doppler ellipse very

Fig. 2.— Latitude- v_{LSR} diagram, constructed by adding three latitude-velocity slices at longitude $l = 137^\circ.865$ and $3'$ offset in longitude on either side. At this longitude, which is slightly offset with respect to the centre of the shell, the slices intersect gas at the most extreme velocity. The ellipse represents the thin shell model fitted in section 3.1, taking into account that the shell is not intersected through the centre in this Figure.

closely. Furthermore, this emission, with velocity -83 km s^{-1} is restricted to the latitude $b \approx -1^\circ 25'$. The emission is therefore not associated with a more widely distributed component, like most of the emission in Figure 2.

The centre, radius, expansion velocity and central velocity of the shell were determined by fitting the velocity field of a thin expanding shell to the data at a number of positions. The line of sight velocity v_{los} for a thin expanding shell with centre (x_c, y_c) , expansion velocity v_0 , radius R_S , and central velocity v_c , at any point (x, y) , with $(x - x_c)^2 + (y - y_c)^2 < R_S^2$, is given by

$$v_{\text{los}} = v_c \pm v_0 \sqrt{1 - \frac{(x - x_c)^2 + (y - y_c)^2}{R_S^2}} \quad (1)$$

The five parameters defining this function can be determined by fitting a large number of measured points (x_i, y_i, v_i) . In particular, the expansion velocity of the shell is determined by on and off-axis data rather than only by emission at the extreme velocities. Similarly, the radius is determined from points over many channels rather than from a single channel map.

The data points (x_i, y_i, v_i) may in principle be distributed anywhere within the radius of the shell, although in practice, there are some restrictions. Measurements well within the outer boundary are required to allow a determination of the expansion velocity. Measurements near the outer boundary of the shell should be avoided, because the component of the expansion velocity along the line of sight vanishes there. Furthermore a degeneracy between the radius and expansion velocity of the shell exists if all measured points are at the same distance from the centre. Data from both sides of the shell are not required, but more accurate results can be expected if data from both the approaching and receding side are included.

Line of sight velocities at 94 positions throughout the area of GSH 138–01–94 were determined by fitting the local line profile with 3 to 5 Gaussians and a second degree polynomial baseline. We are only concerned with obtaining a good fit to the centroid of the one component in the line profile associated with the shell. The remaining components were added to achieve a satisfactory fit to the H I line profile. Only the position and velocity of the Gaussian component identified with the shell were used. The distribution of the measured points on the sky is shown in Figure 3. More data exist for the approaching side of the shell because this side does not suffer from confusion with other emission. The results of the fits (see Table 1) did not change by a large amount when the fit was repeated for five randomly selected subsets containing only one third of the data. The spread in the results from the fits to subsets of the data was used to determine the errors listed in Table 1. The results are consistent within the errors with estimates of the geometric centre and radius defined

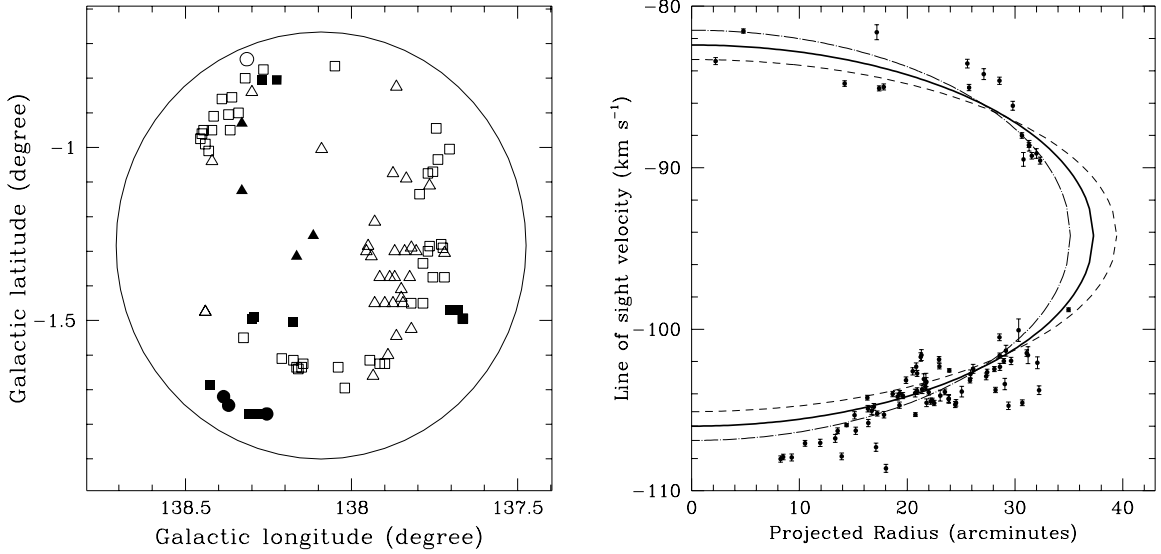


Fig. 3.— *Left*: Locations of data points used for the fit on the sky. Symbols: triangles: $|v_{\text{los}} - v_c| > 10 \text{ km s}^{-1}$, squares: $10 \text{ km s}^{-1} \geq |v_{\text{los}} - v_c| > 5 \text{ km s}^{-1}$, circles: $5 \text{ km s}^{-1} \geq |v_{\text{los}} - v_c| > 0 \text{ km s}^{-1}$. Filled symbols represent the receding (far) side of the shell, open symbols the approaching (near) side. *Right*: Line of sight velocity of shell material as a function of projected distance from the centre. The curved lines are the best fit solution of expression (1) (solid line) and the solutions with 1σ perturbations of radius and expansion velocity (dashed and dot-dashed curves).

Table 1: Properties of GSH 138–01–94 .

Quantity	Value	Reference
Centre (Galactic)	$l = 138^\circ 6' \pm 3' \quad b = -1^\circ 15' 5 \pm 3'$	Section 3.1
Centre (J2000)	$\alpha = 2^{\text{h}} 50^{\text{m}} 35^{\text{s}} 0 \quad \delta = +58^\circ 00' 15''$	
Central velocity	$-94.2 \pm 0.5 \text{ km s}^{-1}$	Section 3.1
Expansion velocity	$11.8 \pm 0.9 \text{ km s}^{-1}$	Section 3.1
Heliocentric distance	$16.6 \pm 2.5 \text{ kpc}$	Section 3.2
Galactocentric distance	24 kpc	Section 3.2
Radius	$37' 3 \pm 2.2$	Section 3.1
	$180 \pm 10 \text{ pc}$	
Mass	$2 \times 10^5 M_\odot$	Section 3.6
Expansion kinetic energy	$3 \times 10^{43} \text{ J}$	Section 3.6
Expansion momentum	$2 \times 10^6 M_\odot \text{ km s}^{-1}$	Section 3.6
Expansion age	$4.3 \times 10^6 \text{ year}$	Section 3.6

by the average and half the difference of the coordinates of opposite sides of the shell in the channel maps.

Adopting the centre derived from the fit, we plot v_{los} as a function of projected distance from the centre in order to display the data and the fit in a 2-dimensional graph. This graph is shown in Figure 3. The data points trace the Doppler ellipse outlined in Figure 2. The scatter in the data exceeds the formal error in the Gaussian fits, and likely reflects departures from the idealized expansion law assumed in equation (1). The solid line represents the best fit to all the data, and the interrupted lines indicate the errors quoted for the radius and expansion velocity. Note that a smaller expansion velocity requires a larger radius to obtain a reasonable fit. The most extreme negative velocities are not very well represented by the fit. These points can be traced to the vertical filament visible in the channel maps around -107.8 km s^{-1} .

3.2. Distance

The central velocity of GSH 138–01–94 is close to the extreme velocity of Galactic H I. This implies a large galactocentric radius for any choice of Galactic rotation curve that is reasonably flat. As many derived properties depend strongly on the adopted distance, a careful review of the uncertainties involved is essential.

The line-of-sight velocity of a cloud on a circular orbit with radius R and velocity $V(R)$ around the Galactic centre assuming circular orbits, is

$$v_{\text{los}} = \left(\frac{R_0}{R} V(R) - V(R_0) \right) \sin l$$

Here, R_0 is the distance of the sun to the Galactic centre, and l is the Galactic longitude of the cloud. This relation can be solved for the Galactocentric distance R , and hence the heliocentric kinematic distance d . For GSH 138–01–94, $v_c = -94.2 \text{ km s}^{-1}$, and $l = 138^\circ 6'$, so $R = 23.6 \text{ kpc}$, and $d = 16.6 \text{ kpc}$, assuming $V(R) = 220 \text{ km s}^{-1}$ and $R_0 = 8.5 \text{ kpc}$.

If GSH 138–01–94 is not at such a large distance, then it must have a high anomalous velocity with respect to the surrounding medium. We rule this out for two reasons. First, the appearance of GSH 138–01–94 on the sky is nearly perfectly circular. This effectively rules out a velocity relative to its immediate surroundings which is a large fraction of the expansion velocity (11.8 km s^{-1}). Second, the mass of GSH 138–01–94 is likely dominated by swept-up interstellar gas. Suppose the source of the shell has a velocity of 100 km s^{-1} relative to the ambient medium, and the mass of the ejecta amounts to 10% of the mass of the shell. Conservation of the momentum of the ejecta due to the velocity of the source,

implies that the peculiar velocity of the shell would be only 10 km s^{-1} in this example.

Of course, this argument does not exclude that the velocity of the surrounding medium is also different from standard Galactic rotation. We now consider localized departures from Galactic rotation along the line of sight, which could create the false impression of a large distance, and departures from standard Galactic rotation in the outer Galaxy.

Large-scale streaming motions in galaxies are associated with bars or spiral arms. Streaming motions associated with spiral arms are the only relevant factor outside the solar circle. The spiral shock model of Roberts (1972) for the longitude range $l = 130^\circ$ to $l = 140^\circ$ allows a minimum line of sight velocity of approximately -55 km s^{-1} , which is some 20 km s^{-1} blueshifted from standard Galactic rotation. The velocity of GSH 138–01–94 is not allowed by the density wave model for the Perseus arm by a margin of 40 km s^{-1} . Also, absorption of radio continuum emission towards the W3/W4 H II regions is not observed beyond $v_{\text{LSR}} = -50 \text{ km s}^{-1}$ (Normandeau 1999). We therefore conclude that the velocity of GSH 138–01–94 implies that it is located well beyond the Perseus arm.

The validity of standard Galactic rotation at large radii is uncertain. The rotation velocity of most spiral galaxies remains nearly constant to the outermost point that can be measured, and the same is true for the Galaxy to a distance $2R_0$ from the centre (Merrifield 1992). By comparison, the kinematic distance of GSH 138–01–94 implies it is $2.8R_0$ from the Galactic centre. The issue concerning the distance to GSH 138–01–94 is not whether the rotation curve of the Galaxy declines at large distances, but rather whether the assumption that the gas follows circular orbits is valid. The magnitude of this effect may be estimated from the $l \rightarrow -l$ asymmetry of the extreme velocity of H I in the Galaxy (Kuijken & Tremaine 1994). The magnitude of this asymmetry is at most 20 km s^{-1} , and the sign implies a more negative velocity in the second quadrant. We estimate the effect of non-circular orbits by adding a radial expansion term of -10 km s^{-1} to the velocity $V(R)$ and recalculating the kinematic distance. The result is a distance which is 3 kpc or 20% smaller than the distance derived assuming circular orbits.

In this paper we therefore adopt a distance of 16.6 kpc for GSH 138–01–94, keeping in mind that a systematic effect of the order of 20% may exist due to non-circular orbits in the outer Galaxy.

3.3. Environment

The large distance of GSH 138–01–94 places it in the far outer Galaxy. The Galactic latitude of its centre corresponds with a distance 370 pc south of the Galactic plane. The

actual centre of the H I layer cannot be determined with a high accuracy for a particular longitude. From Figure 60b in Burton (1991) it is estimated that the centre of the H I layer is between 0.5 and 1 kpc toward positive Galactic latitude in the vicinity of GSH 138–01–94 . The half-width thickness of the Galactic H I layer at 20 kpc from the centre is approximately 1.5 kpc (Merrifield 1992). Therefore, GSH 138–01–94 is not exceptionally far from the local midplane, and its diameter is about a quarter of the thickness of the disk at half maximum. The side of GSH 138–01–94 in the direction of the Galactic equator is a factor two brighter than the side facing the opposite direction, which is consistent with a density gradient perpendicular to the plane.

Adjacent to GSH 138–01–94 at lower longitude an H I complex is observed that may have some connection with GSH 138–01–94 . The H I complex displays a peculiar velocity gradient in the sense that the velocity is more negative at a larger distance from the Galactic equator. For a disk in which the rotation speed does not change with distance from the midplane, the velocity is expected to become less negative by a factor $\cos(b)$, which is negligible over the latitude range considered. Although this H I complex may be physically related to GSH 138–01–94 , it may also be a coincidence because a small velocity interval corresponds with a large distance along the line of sight in this part of the Galaxy.

The gas density in the vicinity of GSH 138–01–94 was derived according to the relation $n_{\text{H}} = N_{\text{HI}}/\Delta d$, with N_{HI} the H I column density obtained by integrating the brightness temperature over a narrow velocity interval Δv centered on the central velocity of the shell. Δd is the length of the line of sight corresponding to Δv and Galactic rotation. The brightness temperature averaged over an area that covers the latitude range of GSH 138–01–94 on both sides in longitude is $T_{\text{b}} = 13$ K, and does not vary significantly with velocity for $\Delta v < 10$ km s^{−1}. The resulting hydrogen density is $n_{\text{H}} = 0.02$ cm^{−3}, which is fairly independent of the particular choice of Δv . This density is within a factor 2 of the azimuthally averaged H I density $n_{\text{H}} = 0.04$ at $R = 2.35R_0$ in Figure 8 of Merrifield (1992). A consequence of the steep slope of the velocity-distance relation for the longitude and velocity of GSH 138–01–94 is that the derived density is the average across a significant line of sight: $\Delta d = 4.7$ kpc for $\Delta v = 10$ km s^{−1}. This will be discussed further in Section 3.6.

3.4. Substructure

At the resolution of 1 arcminute a great deal of substructure is observed. At the most extreme velocity ($v_{\text{LSR}} = -110$ km s^{−1}) a prominent filament is seen in the channel maps. Such condensations and filaments may form as a result of the Rayleigh-Taylor instability if a dense shell is expanding due to the pressure of the tenuous hot interior, and thermal

instabilities because the cooling increases with density. A number of compact spots can be seen in Figure 1, e.g. at $(l, b, v) = (138^\circ.125, -0^\circ.695, -106.2)$.

At $(l, b, v) = (137^\circ.79, -0^\circ.81, -99.6)$ and adjacent channels, a conspicuously empty, $7'.2 \times 4'.2$ elliptical area is visible in the rim of the shell. Over the velocity $-90 \text{ km s}^{-1} > v_{\text{LSR}} > -110 \text{ km s}^{-1}$, the brightness temperature remains below 15 K in this area. This is consistent with the intensity of the surroundings of the shell, and about half the intensity of the bright edge surrounding this area. The isophotes of the hole are elliptical, with major axis in position angle 36° , and axial ratio 0.59. The projected distance of the hole from the centre of GSH 138–01–94 is 0.895 times the radius of the shell in position angle -33° . A circular hole in the shell seen in projection at the same location, would appear as an elliptical hole with its major axis in position angle 33° , and axial ratio 0.45. Taking into account the uncertainties in the positions, the observed shape of the hole is consistent with a nearly circular hole in GSH 138–01–94. At the distance of 16.6 kpc, the diameter of this hole is 35 pc. We refer to this hole as Cavity 1.

A smaller, but very distinct empty region is observed at $(l, b, v) = (137^\circ.54, -1^\circ.05, -101.2)$, and the adjacent channel maps. The central brightness temperature remains consistent with the background, which is a factor 3 below its immediate surroundings. We refer to this feature as Cavity 2.

3.5. Spin temperature

A weak but distinct absorption feature is observed against a $T_b = 82.8 \text{ K}$ background continuum source in the direction $(l, b) = (137^\circ.93, -1^\circ.27)$. Figure 6 A shows the absorption profile in this direction. We determine the peak brightness temperature by fitting a Gaussian and a constant offset to the data in a specific velocity interval. The sum of the Gaussian and the offset is a relatively accurate estimate of the brightness temperature at $v_{\text{LSR}} = -107 \text{ km s}^{-1}$, despite the modest signal to noise ratio of typically 7, because it uses information from more than one channel. This was done for eight positions, $\pm 3'$ offset in longitude or latitude, from the position of the continuum source. The fitted offset in intensity contributes typically less than 20% to the total intensity. The mean brightness temperature at the eight off-positions is $T_{b,\text{off}} = 18.6 \pm 1.3 \text{ K}$. The error indicates the rms variations, divided by $\sqrt{8}$, and is comparable to the formal error in the fit of a single spectrum. At the position of the continuum source the brightness temperature is $T_{b,\text{on}} = 11.9 \pm 1.5 \text{ K}$, which is less than any of the eight surrounding positions. These numbers imply a spin temperature between 173 K and 367 K, for 1σ variation of $T_{b,\text{on}}$ and $T_{b,\text{off}}$, with a most likely value of $T_s = 230 \text{ K}$. The optical depth is 0.084. Although velocity crowding can place unrelated

gas at the same velocity, the fact that we see a narrow absorption feature at this velocity argues against this possibility. We therefore conclude that the spin temperature derived here applies to H I in GSH 138–01–94 .

An upper limit to the kinetic temperature can be derived from the width of the line profiles. The average H I velocity dispersion is 1.9 km s^{-1} for the eight off-positions, with scatter consistent with the formal error of 0.4 km s^{-1} from the fit. Fits at other locations in the shell give a similar result. An upper limit $T_{\text{kin}} < 430 \text{ K}$ to the kinetic temperature is found by assuming that the observed linewidth is completely due to thermal broadening. This upper limit is consistent with the low spin temperature derived above, and emphasizes that the temperature in the shell is not far from the temperature of warm H I in the interstellar medium.

3.6. Mass, energy, momentum

The relatively smooth H I background visible in Figure 1 was subtracted by applying a median filtering procedure outlined in Section 3.7 to the H I channel maps, with one difference. Instead of applying a cutoff in intensity to exclude bright point sources, the brightest parts of the shell were masked manually in each channel map. Inspection of the line profiles next to the brighter parts of GSH 138–01–94 showed that the zero level in the residual data cube is well defined. Some uncertainty is unavoidable because emission of GSH 138–01–94 is blended with the H I cloud on the right hand side of GSH 138–01–94 in the velocity interval -94.6 km s^{-1} to -101.2 km s^{-1} , around longitude $137^\circ 5$.

Summation of the background subtracted data cube between -82.3 km s^{-1} and -115.2 km s^{-1} results in a total H I mass $M_{\text{HI}} = 1.8 \times 10^5 M_\odot$ within a circular area defined by the outline of GSH 138–01–94 . The area bounded by the limits $l < 137^\circ 75$, $b > -1^\circ 45$, and the outer radius of GSH 138–01–94 is affected by confusion with the adjacent cloud (see Figure 1). The H I mass in this area is $4.2 \times 10^4 M_\odot$, or 23% of the total. In order to correct for the presence of the cloud, we assume that the H I mass in the area affected by confusion is equally distributed between the shell and the cloud. With this correction, we find $M_{\text{HI}} = 1.6 \times 10^5 M_\odot$. The atomic hydrogen mass is an order of magnitude larger than the molecular mass discussed in Section 3.8. Taking into account primordial Helium, we find the total mass of GSH 138–01–94 is $M_{\text{tot}} = 1.3 M_{\text{HI}}$. The kinetic energy associated with the expansion of the shell then follows from $E_{\text{kin}} = \frac{1}{2} M_{\text{tot}} v_{\text{exp}}^2$ and the momentum from $P_{\text{exp}} = M_{\text{tot}} v_{\text{exp}}$. Numerical values for these quantities are listed in Table 1.

The hydrogen mass in the volume of the shell assuming the density $n_{\text{H}} = 0.02 \text{ cm}^{-3}$

(Section 3.3) is $1.2 \times 10^4 M_{\odot}$, an order of magnitude smaller than the H I mass of the shell. This difference cannot be the result of an error in the distance. The swept-up mass is proportional to the volume, therefore the third power of distance. The HI mass derived from the lineflux is proportional to the square of the distance. Therefore, a ten times larger distance would have to be assumed to obtain consistent results. The discrepancy can be resolved if the environment of GSH 138–01–94 has a higher density than the Galactic average at the Galactocentric radius of GSH 138–01–94. The density found in Section 3.3 is an average over a long line of sight. If the swept-up mass and the mass of the shell are equal, the density is $n_{\text{H}} = 0.27 \text{ cm}^{-3}$, seven times the average midplane density found by Merrifield (1992). This estimate of the ambient density is preferred over the density derived in Section 3.3, but the uncertainty in the density is at least a factor 2.

The expansion age of GSH 138–01–94 is $\tau_{\text{exp}} = \alpha R/v_{\text{exp}}$, assuming the expansion law $R \sim t^{\alpha}$. We assume $\alpha = \frac{2}{7}$. This is applicable to a shell expanding from the pressure of a hot interior, such as an old supernova remnant (McKee & Ostriker 1977). The expansion age thus becomes $\tau_{\text{exp}} = 4.3 \text{ Myr}$. The precise value of α is of less importance given the uncertainties, but we note that we somewhat underestimate the age in the likely event that the expansion law was steeper in the past.

3.7. Radio continuum

Figure 4 shows the DRAO 74-cm continuum map of the area of GSH 138–01–94. The gradient in the background intensity in Figure 4 is due to the Galactic background emission that decreases with distance from the Galactic equator. There is no indication of enhanced emission, on top of the Galactic background, associated with GSH 138–01–94. In order to derive an upper limit to the continuum flux of GSH 138–01–94, we subtracted the smooth Galactic background emission in the following way.

First, point sources brighter than approximately $T_{\text{b}} = 20 \text{ K}$ above the diffuse background were excluded from the analysis by clipping on intensity. The clipped image was subjected

Fig. 4.— Gray scale representation of the 408 MHz continuum image. Gray scales are linear and range from 50 K (white) to 65 K (black). The location of the H I shell is indicated by the white contour, of the column density $2 \times 10^{20} \text{ cm}^{-2}$, obtained by integration over the velocity range -98 km s^{-1} to -107 km s^{-1} . A + marks the expansion centre of GSH 138–01–94 determined in Section 3.1. The square indicates the field of view of Figure 5.

to a spatial median filter with dimensions $6' \times 90'$ in latitude and longitude, in two steps. In the first step, the median filtered image was subtracted from the original image in order to obtain a first order residual image of structure on scales much smaller than the size of the median filter. This first-order residual image was clipped at the $T_b = 4$ K level, setting all pixels below this level to 0. Only individual point sources exceeded the 4 K level. The clipped first-order residual image was then subtracted from the original image.

In the second step, the median filter was applied to the point source subtracted image. This second pass resulted in our final estimate of the smooth background. The residual image after subtraction of the final smooth background image, has a well-defined zero level. The elongated shape of the median filter allows effective subtraction of structure that is extended in Galactic longitude, while retaining elongated structure oriented at a large angle with respect to the Galactic plane. Negative residuals are less than 7% (typically 2%) of the smooth background emission in the vicinity of GSH 138–01–94. The background subtraction procedure was tested in another area of the CGPS, where continuum shells of the same angular size as GSH 138–01–94 were detected. It was confirmed that a shell structure of the size of GSH 138–01–94 is effectively separated from the background by this procedure. This method, then, effectively allows us to identify a shell in continuum, if it exists. No shell was observed above the noise.

The sensitivity of the DRAO 408 MHz map is limited by confusion of faint background sources. Excluding individually visible point sources, the r.m.s. fluctuations in the residual image are $\Delta T_b = 0.86$ K. Due to the crowding of the many resolved point sources, it is not feasible to integrate the flux over the area of GSH 138–01–94. Instead we adopt the r.m.s. fluctuations of the background as a safe upper limit to the surface brightness. An object with the size of GSH 138–01–94 and brightness temperature $T_b = 0.86$ K (1σ) would have been recognized in the residual map without difficulty. The number of independent beams over the area of GSH 138–01–94 should not be used to quantify the statistical significance of this upper limit, because it does not take into account the many point sources in the

Fig. 5.— Detail of GSH 138–01–94 displaying the area around Cavity 1 indicated by the box in Figure 4. Gray scales represent H I column density, integrated over the velocity range -98 km s $^{-1}$ to -107 km s $^{-1}$. The range of gray scales is 0.6×10^{20} cm $^{-2}$ (white) to 8.0×10^{20} cm $^{-2}$ (black). White contours give the CO brightness temperature integrated over the same velocity range. Contour levels for the CO map are 2 (5σ), 3, 4, 5 K km s $^{-1}$. The 21-cm continuum intensity is shown as black contours at $T_b = 0.14$ (2σ), 0.28, 0.42, ... K above the mean background level of 5.13 K. The + indicates the position of the B1 star studied by De Geus et al. (1993). The peaks in the H α emission are indicated with \times .

field.

The 408 MHz surface brightness is then bounded by $\Sigma_{408} < 4 \times 10^{-23} \text{ W m}^{-2} \text{ Hz}^{-1} \text{ sr}^{-1}$. This upper limit is significant, because it is an order of magnitude below the surface brightness of known old supernova remnants (Landecker et al. 1990). An upper limit to the 408 MHz flux density can be derived from the upper limit to the surface brightness. There is some uncertainty in the choice of the area to which the surface brightness limit applies. A likely possibility is that a radio continuum counterpart of GSH 138–01–94 would have a shell morphology similar to the HI. In this case, the upper limit to the surface brightness is really a limit to the surface brightness of the bright outer rim of such a continuum shell. Assuming a ring with outer radius $37'.3$, inner radius $30'$, and a uniform surface brightness equal to the upper limit translates in an upper limit of 0.57 Jy to the flux density at 408 MHz.

Figure 5 shows the 1420 MHz continuum image of the area indicated by the square in Figure 4. An extended continuum source is seen in projection on the edge of Cavity 1. When rotated by 20 degrees counter clockwise, Figure 5 can be compared directly with Figure 3 in De Geus et al. (1993). Radio continuum emission is observed at the location of the two maxima in $\text{H}\alpha$ intensity in the map of De Geus et al. (1993), as indicated in Figure 5. In fact, the H II region is extended and covers the same area on the sky as the faint resolved 21-cm continuum emission. Based on the correlation with $\text{H}\alpha$ and the absence of a counterpart at 74 cm, the continuum emission may well be thermal emission from the H II region. The velocity of the H II region as determined by De Geus et al. (1993), is -101 km s^{-1} . The H I that can be associated with this H II region and the adjacent molecular cloud (Section 3.8) is part of the edge of Cavity 1, which is a hole in GSH 138–01–94 (Section 3.4).

3.8. Molecular gas

The FCRAO CO data show a small molecular cloud (number 2 in Digel et al. 1994) at $(l, b, v) = (137^\circ.76, -0^\circ.97, -103.6)$, with peak brightness temperature $T_b = 2.9 \text{ K}$, and velocity dispersion $\sigma_{\text{CO}} = 0.94 \text{ km s}^{-1}$. De Geus et al. (1993) found an H II region with the same velocity as the molecular cloud and a candidate ionizing B star with a photometric distance between 17.5 and 32 kpc. The relative locations of the molecular cloud, the H II region and the ionizing star are indicated in Figure 5.

Figure 6 B shows the CO and H I spectra at this position. H I emission at $v_{\text{LSR}} = -101.9 \text{ km s}^{-1}$ is associated with GSH 138–01–94. The H I and CO profiles can be compared directly thanks to the arcminute resolution and zero spacing information in the DRAO

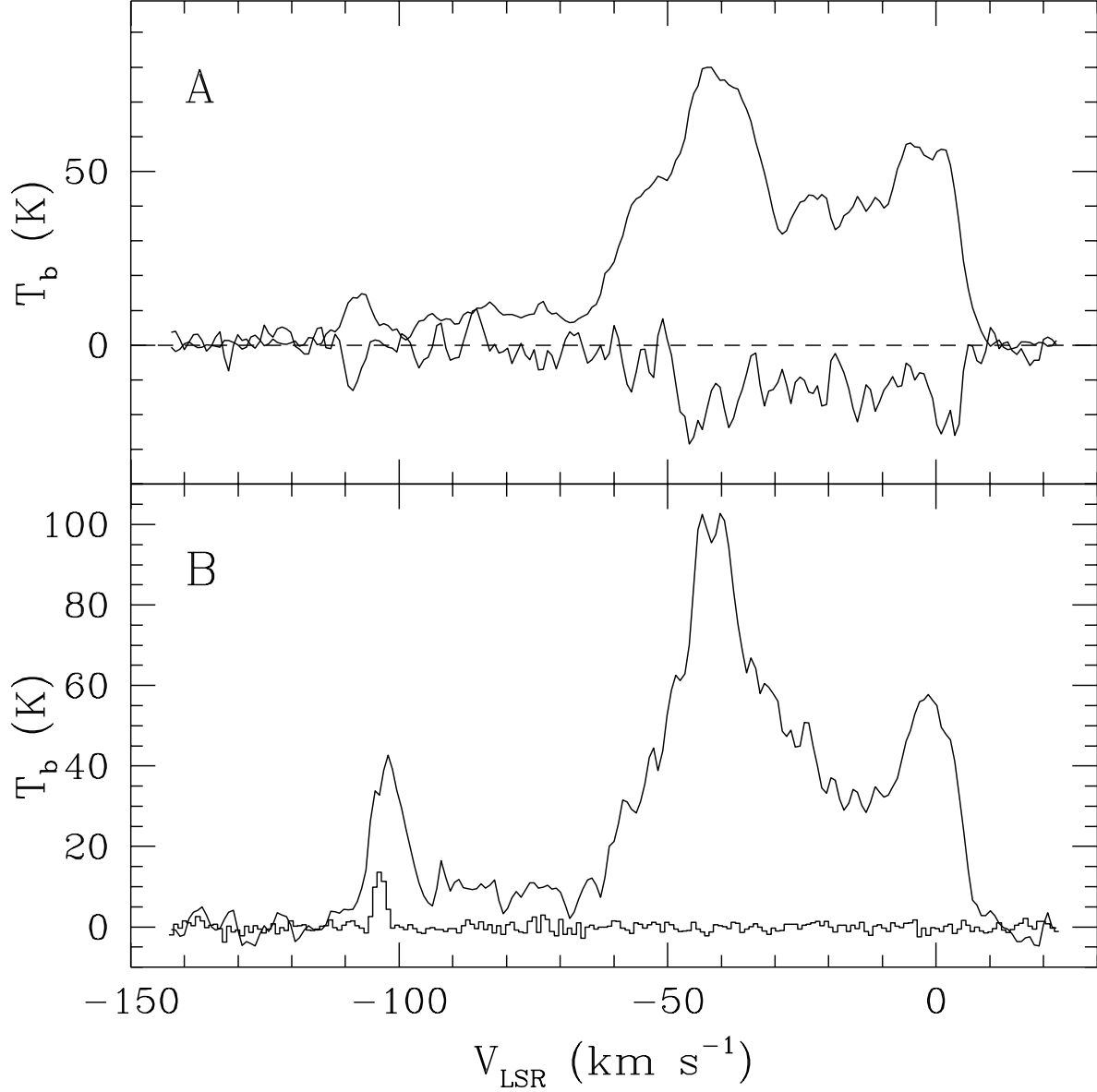


Fig. 6.— A: Absorption of Galactic H I against the continuum source at $(l, b) = (137.93, -1.27)$. The smooth emission spectrum is the average of eight positions 3' offset in l and b . The negative curve is the difference between the spectrum at the position of the continuum source and the average spectrum of the surroundings. Note the absorption feature at $v_{\text{LSR}} = -108$ km s⁻¹, which is associated with GSH 138–01–94. B: CO emission line (histogram) and H I emission in the direction of the CO cloud.

H I data. The coincidence of these two features in position *and* velocity is highly unlikely to be a chance alignment. We therefore associate the CO cloud with the approaching side of the H I shell. Note that this association of the CO cloud with GSH 138–01–94 means its distance is 16.6 kpc (Section 3.2), considerably smaller than the kinematic distance of 21 kpc adopted by Digel et al. (1994). It is noteworthy that cloud 2 is the only one of 11 clouds in the sample of Digel et al. (1994) for which the mass derived from the CO flux exceeds the virial mass. The smaller distance that we derived here, decreases this discrepancy significantly, because the virial mass scales only linearly with distance.

In this interpretation, this molecular cloud is only marginally more distant than the other molecular clouds in the sample of Digel et al. (1994), and only marginally inconsistent with the photometric distance of the B star found by De Geus et al. (1993). Digel et al. (1994) found the mass of this molecular cloud to be $2.3 \times 10^4 M_{\odot}$, assuming a distance of 16.6 kpc. The bright northern rim of the GSH 138–01–94 was targeted by Digel et al. (1994), but no CO emission was found there. Digel et al. (1994) identified the pointsource IRAS 02450+5816 with their cloud 2, but there is no indication of a shell structure in the IRAS maps.

4. Discussion

4.1. Source of the shell

The kinematic distance to GSH 138–01–94 is the basis for our interpretation of the data presented in this paper. Summarizing the arguments given in Section 3.2, we conclude that systematic effects between 10 km s^{-1} and 20 km s^{-1} may exist, but these do not seriously affect our conclusions. We estimate an error in the distance of 20%, similar to the assessment of Digel et al. (1994) for their molecular clouds. The association of the H II region found by De Geus et al. (1993) and a photometric distance of its probable ionizing star with GSH 138–01–94 supports the large distance derived in Section 3.2. The conclusion that GSH 138–01–94 is in the far outer Galaxy does not depend on the exact shape of the rotation curve in the outer Galaxy. The distance of GSH 138–01–94 is therefore sufficiently secure to allow a meaningful comparison with other shells of known origin.

The size of GSH 138–01–94 is similar to small superbubbles, such as the Orion-Eridanus bubble (Brown et al. 1995). However, the kinetic energy of the expanding shell ($3 \times 10^{43} \text{ J}$) is consistent with the 10^{44} J released in a single supernova explosion (Leitherer et al. 1992). Although the expansion energy of GSH 138–01–94 is a factor 3 smaller, this is well within the uncertainty in the energy release of a supernova, and which fraction of this energy is in

the form of kinetic energy of the ejecta. A recent discussion was given in Thornton et al. (1998). The energy released in a stellar wind can be of the same order of magnitude as the kinetic energy of the ejecta of a supernova explosion. We first explore what star could be the source of GSH 138–01–94 assuming the shell is the result of only a stellar wind.

Normandeau et al. (2000) discuss the possible sources of the H I shell G132.6–0.7–25.3 (radius 33 pc). This shell may be a bubble blown by the stellar wind of the B1 Ia star BD60°447, but the expansion age of this shell is less than the age of the star. Normandeau et al. (2000) conclude that G132.6–0.7–25.3 can also be an old supernova remnant. Bransford et al. (1999) found shells with radii up to 80 pc in a survey of Wolf-Rayet stars in M31. Although GSH 138–01–94 is more than twice the size of the largest of these shells, it cannot be excluded that this is the result of a lower ambient density. The most significant parameters for the interpretation of GSH 138–01–94 as a wind blown bubble are the expansion kinetic energy and the age of the shell. The expansion kinetic energy of GSH 138–01–94 is 30 times larger than that of G132.6–0.7–25.3 (Normandeau et al. 2000). Note that Normandeau et al. (2000) found only one star that could have been the origin of G132.6–0.7–25.3 by means of its stellar wind.

The mass loss rate from a stellar wind increases rapidly with luminosity. The longer lifetime of a star with lower mass compensates only partly for the much smaller mass loss rate. The mass loss rate also depends on the metallicity Z . Nugis & Lamers (2000) find that the mass loss rate scales as Z^m , $m = 0.5$. Vink et al. (2001) predict $m = 0.64$ to $m = 0.69$, and argue that oxygen is the relevant trace element for Z at low metallicity. At 18 kpc from the Galactic center, the abundance of oxygen relative to hydrogen is a factor 10 below the solar value (Smartt & Rolleston 1997). The velocity of the stellar wind is also smaller at low metallicity (Nugis & Lamers 2000). We conclude that the energy released in the form of a stellar wind decreases by a factor ~ 3 if the metallicity decreases with a factor 10, for stars with the same luminosity.

The relation between stellar luminosity and the energy released per second in the stellar wind was defined from the sample of O and B stars of Lamers et al. (1999). The lifetime of these stars was related to luminosity at mid-life using the stellar evolution models for solar metallicity of Bressan et al. (1993). From this, a relation was found between luminosity and the total energy released in the stellar wind during the lifetime of the star. The expansion energy of GSH 138–01–94 requires a star with luminosity $\log(L/L_\odot) = 5.7$ at solar metallicity. Assuming the metallicity is 0.1 solar, we find $\log(L/L_\odot) = 5.9$. This luminosity implies a star with main sequence mass $60 M_\odot$, lifetime 4.1 Myr (Bressan et al. 1993), spectral type on the main sequence approximately O5. The same result can be obtained from Abbot (1982). It was implicitly assumed that all of the kinetic energy of the stellar wind is available for the

expansion of the shell. It is more likely that some fraction is converted into thermal energy as the stellar wind and the swept-up interstellar medium pass through a shock. In this case a stronger stellar wind (i.e. a more massive star with a shorter lifetime) would be required. The age of GSH 138–01–94 is 4.3 Myr assuming an expansion law $R \sim t^{2/7}$ (Section 3.1), similar to the lifetime of a $60 M_{\odot}$ star. It is therefore difficult to provide the expansion energy of GSH 138–01–94 in the form of a stellar wind by a star with a lifetime as long as the age of GSH 138–01–94 .

Are the present data consistent with the existence of such a massive star? If the star still exists, thermal emission of an H II region associated with the star should be visible in the 1420 MHz continuum map, which shows only the small H II region found by De Geus et al. (1993) (Figure 5). The effective temperature is lower at a later stage of evolution of the star, but only for a brief period of time. In the models of Bressan et al. (1993) the effective temperature of a star with initial mass $60 M_{\odot}$ is below 3×10^4 K for only 4000 years (0.1% of the lifetime of the star). Assuming an O5V star and the extinction $A_V = 2.7$ mag found by De Geus et al. (1993), we estimate the star should be magnitude $V = 13$, observed color $U - B = -0.5$. With this brightness and color, the star would be an obvious target for the search for blue stars by Lanning (1977). There is no entry in his list near the center of GSH 138–01–94 , although the objects 7 ($m_B \approx 20$) and 54 ($m_B \approx 12.7$) are within the field covered by the channel maps in Figure 1 (but outside the perimeter of the shell).

We conclude that the existence of a star with the mass required by the interpretation of GSH 138–01–94 as a stellar wind bubble is unlikely. The radio continuum maps at 408 MHz and 1420 MHz also show no evidence for a supernova remnant inside GSH 138–01–94 . If the shell is a supernova remnant, the problems raised by the interpretation of GSH 138–01–94 as a stellar wind bubble are resolved. In particular, a less massive star is required than in the stellar wind case.

GSH 138–01–94 is larger and older than known supernova remnants. It is illustrative to compare GSH 138–01–94 with supernova remnants in the solar neighbourhood. The Cygnus Loop has a radius of 19 pc and age 1.4×10^4 yr (Levenson et al. 1998). The Cygnus Loop is therefore of the same size as Cavity 1 (Figure 5). GSH 138–01–94 is larger and older than known supernova remnants. Supernova remnants that are considered to be very old include G55.0+0.3 with radius 70 pc, age 1 Myr (Matthews 1998), G65.2+0.6 with unknown distance but has a low radio surface brightness, (Landecker et al. 1990), G106.3+2.7 with radius 70 pc, age 1.3 Myr (Pineault & Joncas 2000), and G166.2+2.5 with radius 87 pc, age (Routledge et al. 1986). Among the older remnants would also be radio loop I, with radius 60 pc and expansion velocity 25 km s^{-1} (Heiles 1984) yielding an age of 0.7 Myr, assuming this is a single supernova remnant. It is usually difficult to

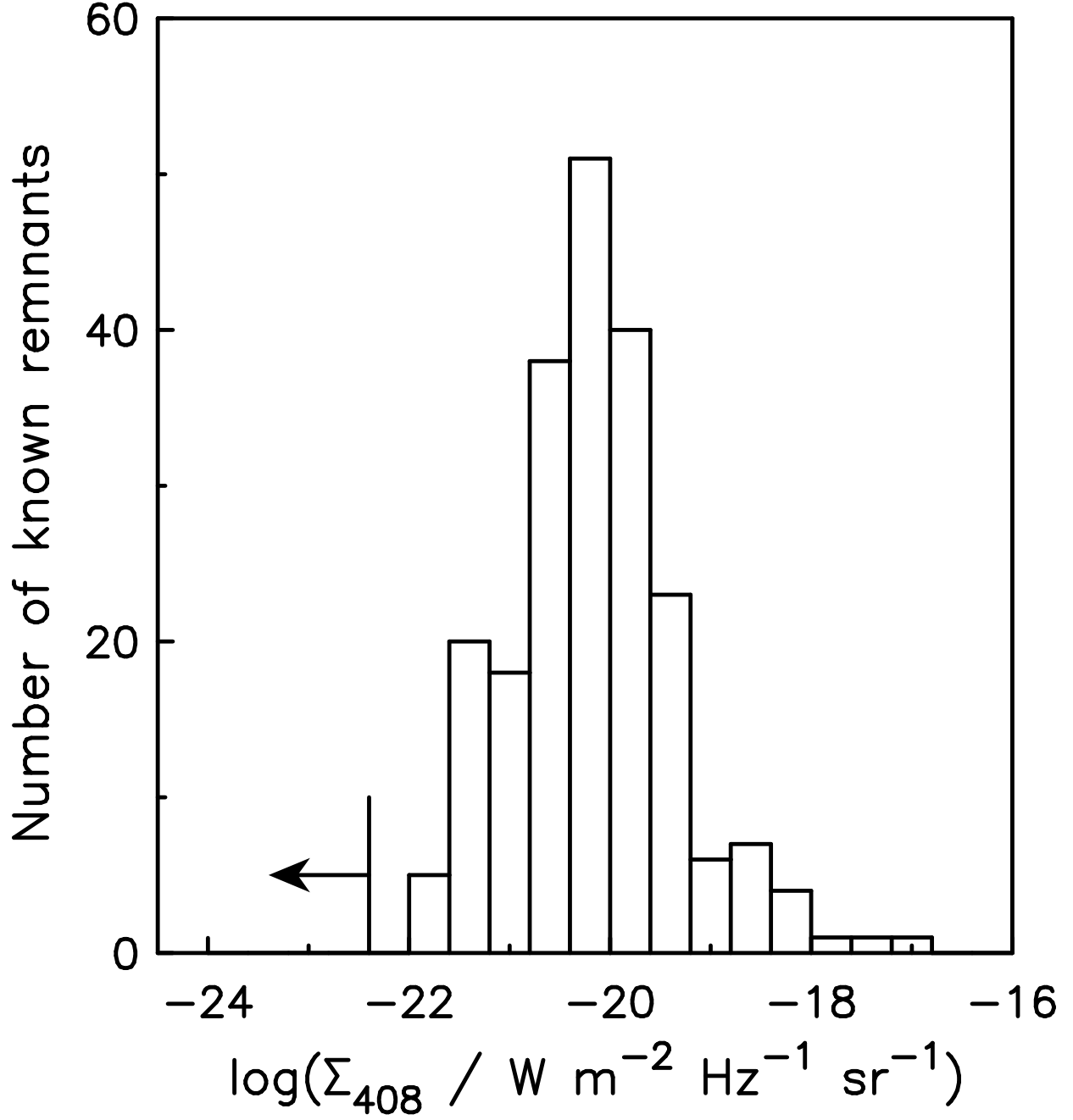


Fig. 7.— Histogram of the number of known supernova remnants as a function of surface brightness at 408 MHz. The arrow indicates the upper limit for GSH 138–01–94 derived in Section 3.7.

estimate the distance of large shells that can be old supernova remnants, and to show that such a shell is the result of a single supernova. Distance ambiguities can be eliminated when looking at nearby galaxies. The largest supernova remnant in the optical spectral line survey of M31 by Blair et al. (1981) is BA 490, with radius 90 pc. Interestingly, BA 490 is located 19 kpc from the centre of M31. Gordon et al. (1999) studied a radio selected sample of supernova remnants in M33, eliminating distance ambiguities. The largest supernova remnants in their sample have radii of 50 pc, but these authors acknowledge a selection effect against the oldest supernova remnants. A direct comparison of GSH 138–01–94 with known supernova remnants is therefore inconclusive because cataloged supernova remnants are significantly younger, smaller and expand faster. This is likely a selection effect because supernova remnants are usually identified in radio or X-ray surveys. As the remnant ages, the radio surface brightness declines and the temperature of the interior drops. From this it cannot be excluded that an older supernova remnant would be similar to GSH 138–01–94, if it managed to survive long enough. In particular, the fact that no radio continuum shell was detected does not disprove the possibility that GSH 138–01–94 could be a very old supernova remnant.

Figure 7 shows the number of known Galactic supernova remnants as a function of radio surface brightness. This histogram is based on the most recent (September 1998) version of the catalogue of Green (1984, 1988) available through the CADC. The surface brightness at 408 MHz was calculated following Green (1991), adopting a spectral index of 0.5 if no spectral index was listed. Six objects out of 220 were excluded because no radio flux was listed. The peak of the histogram corresponds with the completeness limit of radio surveys, as demonstrated in Figure 3 of Green (1991).

It is often assumed that an expanding shell dissolves into the ambient medium if its expansion velocity becomes similar to the random velocity of clouds, which is of the order of 10 km s^{-1} . Clearly this is the case for GSH 138–01–94, but it is still a well-defined shell. The residual velocities in Figure 3 are of the order of 3 km s^{-1} . It is not likely that the velocity dispersion in the outer Galaxy is significantly smaller than 10 km s^{-1} . H I observations of face-on galaxies show that the H I velocity dispersion is nearly 10 km s^{-1} , even far beyond the optical radius (Van Zee & Bryant 1999). The timescale for dissolving into the surrounding medium is of the order of $t_{\text{dis}} = R_S/\sigma_v$, where R_S is the radius of the shell, and $\sigma_v \approx 10 \text{ km s}^{-1}$ is the velocity dispersion of HI clouds. For GSH 138–01–94 we find $t_{\text{dis}} = 18 \text{ Myr}$. McKee & Ostriker (1977) also found that the timescale for the low-density cavity created by a supernova remnant will survive approximately 10 times longer than the timescale to reach equilibrium between the internal and external pressure. Their t_{max} uses the sound speed in the ambient medium, and is of the same order of magnitude as t_{dis} . The long dissolving timescale resolves the apparent contradiction of a well-defined H I shell with

expansion velocity of the order of the velocity dispersion of the ambient interstellar medium.

4.2. GSH 138–01–94 compared with SNR models

Detailed one-dimensional hydrodynamic simulations of the evolution of supernova remnants including a realistic, metallicity-dependent, cooling function were made by Thornton et al. (1998). A proper treatment of cooling is essential for simulations that proceed beyond the adiabatic expansion phase of the remnant. Radiative cooling becomes important first in the relatively dense expanding shell. In the late stages evolution of the supernova shell, the pressure of the hot interior drives the expansion and compresses the shell further, increasing the cooling rate in the shell. This leads to a thin neutral shell in the so-called “pressure driven snow plow phase”. This qualitative scenario is supported by hydrodynamic simulations that include radiative cooling, e.g. Cioffi et al. (1988) and Thornton et al. (1998). The pressure driven snow plow phase continues until the pressure of the hot bubble drops so far that it can no longer drive the expansion of the remnant. Not surprisingly, the timescale for the end of the pressure driven snow-plow phase depends on the cooling rate of the gas, which itself depends on the density, metallicity and temperature. Thornton et al. (1998) included the most detailed cooling function to date and provide relations for the properties of the remnant as a function of age, metallicity and density of the ambient medium.

The density and metallicity of the ambient medium must be assumed in order to compare the models with the observations. The metallicity of the gas is an uncertain factor. Most spiral galaxies show a decline in metallicity with radius (Ferguson et al. 1998b), (Van Zee et al. 1998). Extrapolating the Galactic gradient, with data out to 18 kpc (Smartt & Rolleston 1997), to a galactocentric radius of 24 kpc, results in an oxygen abundance 10% of the solar value. Similar values were found for outlying H II regions in other galaxies (Ferguson et al. 1998b). As oxygen lines contribute significantly to the cooling, the oxygen abundance should be a relevant indicator of the total metallicity parameter in the models. Therefore, we adopt a metallicity of 10% of the solar value.

The scaling relations in Thornton et al. (1998) were used to obtain the model predictions listed in Table 2. The model parameters were chosen to cover the relevant range of density and metallicity and do not represent a fit to the data. The radius of the model is particularly sensitive to the density of the ambient medium. An error of a factor 2 in the density translates into a 50% difference in the radius, whereas a factor 10 in metallicity results in a 20% difference in radius. The mass of the model shells is approximately equally sensitive to density and metallicity (20% for a factor 2 variation). The models show a very good overall agreement with the observations if the density of the ambient medium is a factor ~ 3 lower

than estimated in Section 3.6 ($n_{\text{H}} = 0.27 \text{ cm}^{-3}$). The age of the model with $n_{\text{H}} = 0.09 \text{ cm}^{-3}$ and $\log([Z/Z_{\odot}]) = -1$ is approximately 3 Myr. This is less than the age of GSH 138–01–94, which is consistent with the smaller radius, larger expansion velocity and smaller mass of the model.

The main difference between the models and GSH 138–01–94 is in the mass of the shell, which is a factor 5 larger than the model predictions. However, in view of the uncertainty in separating emission of GSH 138–01–94 from unrelated Galactic emission, the distance to GSH 138–01–94, the energy release of a supernova explosion adopted in the models, the assumed metallicity, and the ambient density, this is not a major problem. We conclude that the observed parameters of GSH 138–01–94 are consistent with those of a very old remnant of a single supernova explosion. We note that occasionally supernovae this far from the Galactic centre must occur, in view of the evidence for stars as early as spectral type B1 in this part of the Galaxy, e.g. De Geus et al. (1993).

The interpretation of GSH 138–01–94 as a supernova remnant makes it the oldest and the largest supernova remnant known. This emphasizes the significance of high-resolution H I surveys as a means to find the oldest supernova remnants. It may not be a coincidence that such an old but intact supernova remnant is found in the outer galaxy, which is an environment very different from that near the solar circle. Individual supernova remnants lose their identity when the shock speed drops below the sound speed of the interstellar medium, or when they intersect with neighbouring supernova remnants (Ilovaisky et al. 1974). The timescale for these effects are expected to be longer in the outer Galaxy because the density of the interstellar medium is smaller, and supernovae are relatively rare. Also, the half-width of the H I disk at 24 kpc is 1.5 kpc, as opposed to 200 pc near the solar circle. Therefore, an expanding shell in the outer Galaxy can grow a factor 5 larger before it bursts out of the disk and loses its identity as a shell (Mac Low & McCray 1988; English et al. 2000).

Observations of GSH 138–01–94 at wavelengths other than the 21-cm line of H I would be of great value to verify its nature. The significance of the non-detection in the IRAS maps is not clear. Emission by dust in the foreground is strong, and far infrared emission of the shell may be weak because of a high gas-to-dust ratio and low interstellar radiation field in the outer Galaxy. There is no feature at the position of GSH 138–01–94 in the 34.5 MHz survey of Dwarakanath & Undaya Shankar (1990), or in the 22 MHz survey of Roger et al. (1999). However, the upper limit to the flux density of GSH 138–01–94 at 408 MHz (0.57 Jy) implies a 34.5 MHz flux density less than 7 Jy at 34.5 MHz, assuming a spectral index of 1. Therefore, the confusion-limited sensitivity of these surveys is insufficient to expect a detection, and more sensitive observations are needed. X-ray emission may be

expected from a hot bubble inside the neutral shell. Figure 7 in Thornton et al. (1998) suggests a temperature for the interior that is within a factor 3 of 10^6 K. The thermal bremsstrahlung spectrum emitted by the hot interior is therefore expected to cut off at a photon energy of a few tenths of keV. With a foreground HI column density $6.3 \times 10^{21} \text{ cm}^{-2}$, these soft X-rays will be heavily obscured. No optical line emission is expected because the luminosity of the Thornton et al. (1998) models is less than 0.5% of the peak luminosity in this late stage of evolution. Arguably the strongest confirmation of a supernova origin of GSH 138–01–94 would be the identification of a central compact object. However, no steep-spectrum continuum source could be identified as a pulsar candidate. A source with an inverted spectrum was noticed at $(l, b) = (138^\circ 198, -1^\circ 290)$, but this may well be an extragalactic object. Finally, the ongoing arcminute resolution H I surveys of the Galactic plane provide the best opportunity to identify similar objects in the far outer Galaxy.

4.3. Interaction with the environment

The side of GSH 138–01–94 which faces the Galactic equator is a factor 2 brighter than the opposite side. This asymmetry translates directly into a factor 2 in density, consistent with a density gradient perpendicular to the Galactic equator. This raises the question whether the circular shape of GSH 138–01–94 is consistent with this overall asymmetry. An estimate of the asymmetry that should be expected can be made by applying the expansion law in Thornton et al. (1998), Equation (20). Keeping all parameters constant except the ambient density n , we have $R \sim n^{-0.42}$. Assume that the northern part of GSH 138–01–94 expanded in a medium with a density that is on average twice the density of the medium on the southern side. Normalizing density and radius to the values in the direction of the gradient (south), we have $n_1 = 1$, $R_1 = 1$, in the direction of the density gradient. Scaling with density, we find $n_2 = 2$, $R_2 = 0.747$ in the opposite direction, and $n_3 = 1.5$, $R_3 = 0.843$ for the direction perpendicular to the density gradient. We therefore estimate the axial ratio to be $2R_3/(R_1 + R_2) = 0.97$. The North-South asymmetry in brightness is therefore consistent with the nearly circular shape of GSH 138–01–94.

The cavities in the upper right quadrant of GSH 138–01–94 discussed in Section 3.4 may be smaller, presumably younger, shells. Cavity 1 is similar in size to the Cygnus Loop. The H II region found by De Geus et al. (1993) is located on the south-eastern edge of Cavity 1. This is also the region where GSH 138–01–94 appears to make contact with an H I cloud (Figure 1). The interpretation of Cavity 1 as a hole in GSH 138–01–94, and the H II region on the perimeter of Cavity 1 is suggestive of progressive star formation. McKee & Ostriker (1977) proposed that the passage of a dense cloud through the shell would leave a hole in

an expanding shell in the snow plow phase, as if casting a shadow. If this were the case, we would expect to observe this cloud. The only candidate, cloud 2 in Digel et al. (1994) is much smaller than Cavity 1 (Figure 5). The absence of a radio continuum counterpart of both Cavity 1 and Cavity 2 argues against the interpretation that these are young supernova remnants. It was argued in Section 4.1 that the non-detection of radio continuum emission does not rule out that it is a supernova remnant because of its large age.

4.4. Implications for galaxies

We have argued that the outer Galaxy is a less hazardous environment for supernova remnants because radiative cooling proceeds at a lower rate, the supernova rate is lower, and the scale-height of the gas disk is larger, than in the inner Galaxy. A similar environment is usually found in the outskirts of other spiral galaxies, and almost everywhere in dwarf irregular and low surface brightness galaxies. GSH 138–01–94 may be the prototype of a class of supernova remnant that is representative for such a low metallicity, low density environment. The timescale to dissolve completely into the interstellar medium when the expansion halts, $t_{\text{dis}} = R_S/\sigma_v$ is of the order of 10 Myr. Assuming this process recently started in GSH 138–01–94, at the age of 4.3 Myr, it becomes clear that the shell will remain as large density enhancement between 5 and 10 Myr after the supernova explosion. We speculate that such old supernova shells may be an important source of dense clouds in a low-density environment. This allows star formation to progress for a long time after a single trigger event.

An expanding shell like GSH 138–01–94 would not be resolved in most studies of the H I velocity dispersion in galaxies outside the local group, but it would fill a significant part of the beam. This may lead to a broader local H I profile, without a counterpart in the optical or radio continuum.

5. Conclusions

GSH 138–01–94 is a large H I shell at a Galactocentric radius of 24 kpc (heliocentric distance 16.6 kpc). Its radius (180 ± 10 pc) and expansion velocity (11.8 ± 0.9 km s^{−1}) suggest an age of 4.3 Myr, assuming the expansion law $R \sim t^{2/7}$. The total mass of the shell is 2×10^5 M_⊙, and the kinetic energy of the expansion is 3×10^{43} J. Stellar wind and a supernova explosion are considered as possible sources of the shell.

If GSH 138–01–94 is a stellar wind bubble, the expansion energy of GSH 138–01–94 sets

a strong lower limit $60 M_{\odot}$ to the mass of the star if the expansion is driven only by a stellar wind. The H II region associated with such a star would have been detected in the radio continuum map at 1420 MHz, or optically. There is also no evidence for a young supernova remnant inside the H I shell.

These objections do not exist if GSH 138–01–94 is a supernova remnant. The properties of GSH 138–01–94 correspond well with hydrodynamic models of supernova remnants in a late stage of evolution. GSH 138–01–94 is then the oldest and largest supernova remnant known. Its large size and age may be related to a low-density, low-metallicity environment.

This work has been supported by the Natural Sciences and Engineering Research Council of Canada (NSERC) for JI, and also by NSERC support towards Canadian Galactic Plane Survey postdoctoral fellowships. JMS is guest user, Canadian Astronomy Data Centre, which is operated by the Herzberg Institute of Astrophysics, National Research Council of Canada. The authors thank the anonymous referee for useful comments on the manuscript.

REFERENCES

- Abbot, D. C. 1982, *ApJ*, 263, 723
- Bransford, M. A., Thilker, D. A., Walterbos, R. A. M., & King, N.L. 1999, *AJ*, 118, 1635
- Blair, W. P., Kirshner, R. P., & Chevalier, R. A. 1986, *ApJ*, 247, 879
- Bressan, A., Fagotto, F., Bertelli, G., & Chiosi C. 1993, *A&AS*, 100, 647
- Brown, A. G. A., Hartmann, & D., Burton, W. B. 1995, *A&A*, 300, 903
- Burton, W. B. 1991, in *The Galactic Interstellar medium*, Saas-Fee course 21, eds. Burton W.B., Elmegreen B.G., Genzel R.
- Carpenter, J. M. 1997, *ApJS*, 115, 241
- Cioffi, D. F., McKee, C. F., & Bertschinger, E. 1988, *ApJ*, 334, 252
- Digel, S., De Geus, E., & Thaddeus, P. 1994, *ApJ*, 422, 92
- Dwarakanath, K. S., Undaya Shankar, N. 1990, *JApA*, 11, 323
- English, J., Taylor, A. R., Mashchenko, S. Y., Irwin, J. A., Basu, S., & Johnstone, D. 2000, *ApJ*, 533, L25

- Ferguson, A. M. N., Wyse, R. F. G., Gallagher, J. S., & Hunter, D. A. 1998a, *ApJ*, 506, L22
- Ferguson, A. M. N., Gallagher, J. S., & Wyse, R. F. G. 1998b, *AJ*, 116, 673
- De Geus, E. J., Vogel, S., Digel, S. W., & Gruendl, R. A. 1993, *ApJ*, 413, L97
- Gordon, S. M., Duric, N., Kirshner, R. P., Goss, W., & Viallefond, F. 1999, *ApJS*, 120, 247
- Green, D. A. 1984, *MNRAS*, 209, 449
- Green, D. A. 1988, *Ap&SS*, 148, 3
- Green, D. A. 1991, *PASP*, 103, 209
- Heiles, C. 1984, *ApJS*, 55, 585
- Heyer, M. H., Brunt, C., Snell, R. L., Howe, J. E., Schloerb, F. P., & Carpenter, J. M. 1998, *ApJS*, 115, 241
- Higgs, L. A. 1999, in *ASP Conf. Ser. 168, New Perspectives on the Interstellar Medium*, ed. A. R. Taylor, T. L. Landecker, G. Joncas (San Francisco: ASP), 15
- Hunter, D. A., Wilcots, E. M., Van Woerden, H., Gallagher, J. S., & Kohle, S. 1998, *ApJ*, 495, L47
- Hunter, D. A., Van Woerden, H., & Gallagher, J. S. 1999, *AJ*, 118, 2184
- Ilovaisky, S. A., & Lequeux, J. 1974, *A&A*, 20, 347
- Kuijken, K., & Tremaine, S. 1994, *ApJ*, 421, 178
- Lamers, J. G. L. M., Haser, S., De Koter, A., & Leitherer, C. 1999, *ApJ*, 516, 872
- Landecker, T. L., Clutton-Brock, M., & Purton, C. R. 1990, *A&A*, 232, 207
- Lanning, H. H. 1973, *PASP*, 85, 70
- Leitherer, C., Robert, C., & Drissen, L. 1992, *ApJ*, 401, 596
- Levenson, N. A., Graham, J. R., Keller, L. D., & Richter, M. J. 1998, *ApJS*, 118, 541
- Matthews, B. C., Wallace, B. J., & Taylor, A. R. 1997, *ApJ*, 493, 312
- Merrifield, M. R. 1992, *AJ*, 103, 1552
- Mac Low, M.-M., & McCray, R. 1988, *ApJ*, 324, 776

- McKee, C. F., & Ostriker, J. P. 1977, *ApJ*, 218, 148
- Normandeau M., 1999, *AJ* 117,2440
- Normandeau M., Taylor, A.R., Dewdney, P. E., & Basu, S. 2000, *AJ* 119,2982
- Nugis, T., & Lamers, H. J. G. L. M. 2000, *A&A*, 360, 227
- Pineault, S., & Joncas, G. 2000, *AJ*, 120,3218
- Routledge, D., Landecker T. L., & Vaneldik, J. F. 1986, *MNRAS*, 221, 809
- Roberts, W. W. 1972, *ApJ*, 173, 259
- Roger, R. S., Costain, C. H., Landecker, T. L., & Swerdlyk, C. M. 1999, *A&AS*, 137, 7
- Sellwood, J. A., & Balbus, S. A. 1999, *ApJ*, 511, 660
- Smartt, S. J., & Rolleston, W. R. J. 1997, *ApJ*, 481, L47
- Taylor, A. R. 1999, in *ASP Conf. Ser. 168, New Perspectives on the Interstellar Medium*, ed. A. R. Taylor, T. L. Landecker, G. Joncas (San Francisco: ASP), 3
- Thornton, K., Gaudlitz, M., Janka, H.-Th., & Steinmetz, M. 1998, *ApJ*, 500, 95
- Vink, J. S., De Koter, A., & Lamers, H. J. G. L. M. 2001, *A&A*, 369, 574
- Van Zee, L., Salzer, J. J., Haynes, M. P., O'Donoghue, A. A., & Balonek, T. J. 1998, *AJ*, 116, 2805
- Van Zee, L., & Bryant, J. 1999, *AJ*, 118, 2172

Table 2: Properties of GSH 138–01–94 compared with model predictions derived from the scaling relations in Thornton et al. (1998). The energy released by the supernova was assumed to be 10^{44} J. The properties of GSH 138–01–94 are given on the last line.

n_{H} (cm^{-3})	$\log([Z/Z_{\odot}])$	R_{S} (pc)	v_0 (km s^{-1})	$\log(M_{\text{tot}}/M_{\odot})$
0.03	−1.0	242.44	14.36	4.76
0.03	0.0	192.57	11.67	4.49
0.09	−1.0	152.83	14.20	4.64
0.09	0.0	121.40	11.55	4.37
0.27	−1.0	96.34	14.05	4.53
0.27	0.0	76.53	11.42	4.26
0.27	−1.0 ^a	180±10	11.8±0.9	5.3±0.3

^aMetallicity estimated from the Galactic oxygen abundance gradient (Smartt & Rolleston 1997).

This figure "figure1.jpg" is available in "jpg" format from:

<http://arXiv.org/ps/astro-ph/0108368v1>

This figure "figure2.jpg" is available in "jpg" format from:

<http://arXiv.org/ps/astro-ph/0108368v1>

This figure "figure4.jpg" is available in "jpg" format from:

<http://arXiv.org/ps/astro-ph/0108368v1>

This figure "figure5.jpg" is available in "jpg" format from:

<http://arXiv.org/ps/astro-ph/0108368v1>